AIP The Journal of Chemical Physics

Numerical approaches to determine the interface tension of curved interfaces from free energy calculations

A. Tröster, M. Oettel, B. Block, P. Virnau, and K. Binder

Citation: J. Chem. Phys. **136**, 064709 (2012); doi: 10.1063/1.3685221
View online: http://dx.doi.org/10.1063/1.3685221
View Table of Contents: http://jcp.aip.org/resource/1/JCPSA6/v136/i6
Published by the American Institute of Physics.

THE JOURNAL OF CHEMICAL PHYSICS **136**, 064709 (2012)

Numerical approaches to determine the interface tension of curved interfaces from free energy calculations

A. Tröster,[1,2,a)] M. Oettel,[2] B. Block,[2] P. Virnau,[2] and K. Binder[2]
[1]Vienna University of Technology, Wiedner Hauptstrasse 8-10/136, A-1040 Vienna, Austria
[2]Johannes Gutenberg Universität Mainz, Staudingerweg 7, D-55099 Mainz, Germany

(Received 19 December 2011; accepted 26 January 2012; published online 14 February 2012)

A recently proposed method to obtain the surface free energy $\sigma(R)$ of spherical droplets and bubbles of fluids, using a thermodynamic analysis of two-phase coexistence in finite boxes at fixed total density, is reconsidered and extended. Building on a comprehensive review of the basic thermodynamic theory, it is shown that from this analysis one can extract both the equimolar radius R_e as well as the radius R_s of the surface of tension. Hence the free energy barrier that needs to be overcome in nucleation events where critical droplets and bubbles are formed can be reliably estimated for the range of radii that is of physical interest. It is found that the conventional theory of nucleation, where the interface tension of planar liquid–vapor interfaces is used to predict nucleation barriers, leads to a significant overestimation, and this failure is particularly large for bubbles. Furthermore, different routes to estimate the effective radius-dependent Tolman length $\delta(R_s)$ from simulations in the canonical ensemble are discussed. Thus we obtain an instructive exemplification of the basic quantities and relations of the thermodynamic theory of metastable droplets/bubbles using simulations. However, the simulation results for $\delta(R_s)$ employing a truncated Lennard–Jones system suffer to some extent from unexplained finite size effects, while no such finite size effects are found in corresponding density functional calculations. The numerical results are compatible with the expectation that $\delta(R_s \to \infty)$ is slightly negative and of the order of one tenth of a Lennard–Jones diameter, but much larger systems need to be simulated to allow more precise estimates of $\delta(R_s \to \infty)$. *© 2012 American Institute of Physics*. [http://dx.doi.org/10.1063/1.3685221]

I. INTRODUCTION

The purpose of the present paper is a thorough analysis of the droplet model approach to determine the free energy barrier for the formation of a (spherical) liquid droplet in a (supersaturated) vapor. According to the picture of classical (conventional) nucleation theory, this barrier results from the competition between the bulk free energy gain proportional to the created droplet volume and the accompanying free energy loss due to the necessary formation and subsequent increase of an interface (see, e.g., Refs. 1–5 for reviews). Unfortunately, in an *infinite* grand-canonical system with short-range interaction between particles, such a state is not well-defined within rigorous thermodynamics.[6,7] A super-saturated vapor, which one may produce by a sudden shift of the chemical potential away from its equilibrium saturation value, does not correspond to a stable state, but is metastable, i.e., only stable on a certain time-scale.

On the other hand, in a *canonical* system of *finite* linear dimension L, at fixed total density a condensed droplet surrounded by (slightly) supersaturated vapor having a chemical potential difference to the equilibrium coexistence value *can* exist as an equilibrium state. A detailed phenomenological analysis of the stability of such states was given in Ref. 8. Note that in this ensemble, in which—besides the temperature—L and ρ are fixed, the measured chemical potential $\mu = \mu_L(T, \rho)$ is the average of a fluctuating variable which explicitly depends on the linear dimension L in addition to the temperature T and the average density ρ. Particles can be exchanged between the droplet and its environment only inside the box, and so at fixed ρ the average μ_L is the same inside and outside of such a droplet (which is geometrically defined by some reasonable criterion), as was explicitly tested using the Widom particle insertion method in Ref. 9. This idea is at the heart of our approach to simulate such equilibrium droplets in order to determine nucleation free energy barriers.[10] Our chosen method replaces the ill-defined grand-canonical equilibrium scenario by the well defined equilibrium canonical scenario. In the finite box, the thermodynamic potential per volume (called $f_L(T, \rho)$ here) is a well-defined observable, and satisfies the relation

$$\left(\frac{\partial f_L(T, \rho)}{\partial \rho}\right)_{T,L} = \mu_L(T, \rho). \tag{1}$$

One could loosely say that for phase-separated states the behavior of the chemical potential $\mu_L(T, \rho)$ is reminiscent of a distorted "van der Waals loop" when plotted against ρ (see Figs. 2 and 3), even though such a statement, which refers to a mean field picture, is certainly misleading to some extent in the present context (cf. Refs. 11 and 12). The precise functional form of $\mu_L(T, \rho)$ depends crucially on the boundary conditions chosen for the simulation, but generally one observes a "back-bent" region confined between a local maximum $\mu_L^{(\max)}(T)$ and a local minimum $\mu_L^{(\min)}(T)$. In this region (with an average density between the densities of the

---

[a)] Electronic mail: troestea@uni-mainz.de.

coexisting bulk vapor and liquid phases), the densities of these associated coexisting phases can be inferred from the equality of their chemical potential with μ_L (Ref. 10).

Of course, by this change of ensemble, the original difficulty of the nucleation approach is not eliminated. For fixed T and ρ, the deviations of the canonical chemical potential $\mu_L(T,\ \rho)$ from its grand-canonical equilibrium counterpart can be shown to vanish with some negative power of L for growing system sizes.[10] In other words, it is impossible to take the thermodynamic limit at *fixed* $\mu \neq \mu_\infty(T,\ \rho)$. This difficulty is due to the fact that the grand-canonical description of nuclei in a super-saturated bulk is thermodynamically *ill-defined*, as there is no rigorous way to define a droplet in any kind of equilibrium with its supersaturated vapor. Rather, this situation may only be thought of as an instantaneous snapshot taken during an—intrinsically *kinetic*—nucleation *process*.[13,14] Moreover, this means that we have to be prepared to live with (hopefully small) finite-size effects that usually accompany a change of ensembles for finite systems.

Following the standard description of Gibbs which we will review in necessary detail below, the excess free energy of a droplet corresponding to these densities can be determined for any choice of the dividing surface. In evaluating our simulation results, it is now crucial to understand that Gibbs' theory does not prescribe any such choice. Thus, we are left with the question which dividing surface to choose to obtain results which are relevant for application to nucleation theory. We will discuss these issues in detail below. At this point it suffices to note the following. For a one-component system, the choice which probably comes closest to the intuitive picture of a "droplet volume" is the so-called equimolar surface, which will be defined later. From the point of view of nucleation theory, however, this choice is not particularly well-suited, as its radius R_e is not directly related to the radius of the critical nucleus R^*, which is determined from the stationarity condition on the radius-dependent grand potential. Due to lack of information on the precise analytical structure of the curvature-dependent interface tension $\sigma(R)$ entering this equation, one frequently resorts to the *capillarity approximation* $\sigma(R^*) \approx \sigma_\infty$, which effectively amounts to completely neglecting the unknown curvature dependence altogether. Unfortunately, such errors enter exponentially in, e.g., the standard formulas for calculating nucleation rates.[1–5,13,14]

To go beyond this crude assumption means to determine $\sigma(R_s)$ for the radius R_s corresponding to the *surface of tension*, which does coincide with R^* even if $\sigma = \sigma(R)$ is allowed to depend on the curvature.

From the theoretical point of view, even though the first seminal papers were published more than 60 years ago,[15–17] the determination of the analytical structure of $\sigma(R)$ continues to be a highly controversial subject. As already indicated by the above discussion, the central object to study is the difference $\delta(R_s) := R_e - R_s$, whose limit δ under extrapolation for $R_s \to \infty$ has become famous under the name *Tolman length*. In particular, Tolman proposed the parametrization,[17]

$$\sigma(R) = \frac{\sigma_\infty}{1 + 2\delta/R}, \tag{2}$$

However, this result is only obtained with the use of several assumptions and approximations, and the actual value of δ for a given system as well as the validity of this parametrization as a whole has been debated continuously in the literature (see Refs. 18 and 19 and references therein).

In contrast to analytic approaches, in our simulations we do not rely on any particular analytical form of $\sigma(R)$, as we only need to determined R_s and $\sigma(R_s)$ numerically to be able to calculate the nucleation free energy barrier from the excess of the grand potential (cf., e.g., Appendix 2 of Ref. 3). Nevertheless, once this is done, it is still interesting to extract information on $\delta(R_s)$ from our simulations, thus helping to clarify the validity of the ansatz (2). Before we discuss how to do this, let us review the concepts of excess free energies, dividing surfaces and the various assumptions in general and try to disentangle the various approximations and assumptions made.

The paper is organized as follows. We first summarize our perspective of the phenomenological theory of the radius-dependent surface tension and the Tolman length. Then we present an application to the Lennard–Jones fluid using results from recent Monte Carlo simulations, and explain how both R_e, R_s and $\delta(R_s)$ can be extracted from these simulation data. However, we find that the analysis is hampered by large (and unexplained) finite size effects. We show that a density functional approach treating interparticle attractions in a mean field manner and enforcing radially symmetric density profiles does not suffer from this problem to such an extent. The paper ends with a summary and discussion of our results.

II. REVIEW OF THE GIBBS DIVIDING SURFACE APPROACH TO PHASE SEPARATION

The purpose of this section is to sketch the main ideas of the classical Gibbs dividing surface approach to phase separation for inhomogeneous fluid/vapor systems. A few comments are in order. First of all, we are aware that a number of excellent references, e.g., Refs. 3 and 20–23 are available on this subject. Nevertheless we feel that it may be useful to provide a complementary accessible review, in which we put particular emphasis on those aspects of the theory that our latter numerical analysis will make heavy use of. In this guided tour through the above references, we also avoid all complications arising from any demand to cover the problem in full generality. For instance, we will concentrate on the case of a simple one-component fluid. Moreover, we follow standard practice to ignore the caveat that a droplet of finite size coexisting in (unstable) equilibrium with surrounding metastable vapor is not a well-defined problem of equilibrium statistical mechanics.

Consider the intuitive idea of a "cluster" of a phase α surrounded by a phase β in a simple fluid. On average, such a cluster may appear to be spherical, but of course its shape may fluctuate and its surface may be rather diffuse. At least on molecular length scales, any attempt to define a cluster volume or surface by a suitably chosen "cluster criterion" thus clearly involves a certain amount of arbitrariness as to which molecules to include/exclude. A corresponding arbitrariness also persists in the analysis of the continuous density profile $\rho(\boldsymbol{x})$ obtained by averaging over individual molecular configurations. On average the gradients of the density profiles $\rho(\boldsymbol{x})$ of phase-separated configurations reflect the spatial symmetry of the underlying phase-separated regions, but the corresponding leveling surfaces of constant density provide a whole family of reasonable candidates for defining an "interface" between phases. Gibbs' approach cuts this Gordian knot by arbitrarily selecting a suitable so-called "dividing surface" A from this family and subsequently exploits the requirement of invariance of thermodynamic observables under a corresponding change of the location of the dividing surface. The price to pay is that many quantities of interest will pick up a "superficial" dependence on the choice of position of the dividing surface, which must be removed from physical observables by exploring the invariance of physical observables under a so-called "notional" change of A, as we explain below.

Once a dividing surface has been chosen, this yields a separation

$$V = V_\alpha + V_\beta, \tag{3}$$

of the total volume. Well inside the bulk phases, the local density $\rho = \rho(\boldsymbol{x})$ should assume its coexistence equilibrium values ρ_α, ρ_β. Pretending these densities to be homogeneous right up to the dividing surface, we *define* the associated numbers of particles in the bulk phases $N_\alpha := V_\alpha \rho_\alpha$, $N_\beta := V_\beta \rho_\beta$ and correct for the error thus introduced in the total particle number N by introducing an *excess* particle number N^x with respect to the partitioning (3) as

$$N \equiv N_\alpha + N_\beta + N^x, \tag{4}$$

such that

$$N^x = \int_{V_\alpha} (\rho(\boldsymbol{x}) - \rho_\alpha) d^3x + \int_{V_\beta} (\rho(\boldsymbol{x}) - \rho_\beta) d^3x. \tag{5}$$

In a similar way, we may form excess contributions of other extensive physical quantities. Of particular importance are thermodynamic excess potentials like U^x, S^x, F^x, Ω^x corresponding to the internal energy U and entropy S, the Helmholtz free energy F, and the grand potential Ω. In the case of a planar interface geometry, the Gibbs dividing surface will of course be chosen to be oriented parallel to the inhomogeneous density region between the two coexisting phases. For the planar geometry, we now notice that the excess Ω^x of the *grand potential* plays a distinct role among all excess potentials, as it is easy to see that Ω^x is *invariant* under a parallel shift of the position of the dividing surface. In fact, such an independence is guaranteed for any quantity whose volume density coincides in both phases. The densities ω_α, ω_β of the grand potentials Ω_α, Ω_β are simply the negative bulk pressures $-p_\alpha$, $-p_\beta$, and these must be equal in the case of a planar interface for stability reasons. The *interface tension* σ is thus well-defined by the relation

$$\sigma \cdot A \equiv \Omega^x = \Omega - \Omega_\alpha - \Omega_\beta, \tag{6}$$

for the case of a planar interface, i.e., $\sigma = \sigma(T, \mu)$ regardless of the normal distance of the dividing surface to the inhomogeneous density region.

Thermodynamically, the identity of pressures $p_\alpha = p_\beta$ for a planar interface follows from the possibility that for such a geometry it is possible to scale both subvolumes V_α, V_β and their interface A by a common factor λ and make use of the bulk extensivity properties and the accompanying Euler relations. It is crucial to realize that this is no longer possible in the presence of a *spherical* interface, and thus the difference in bulk pressures

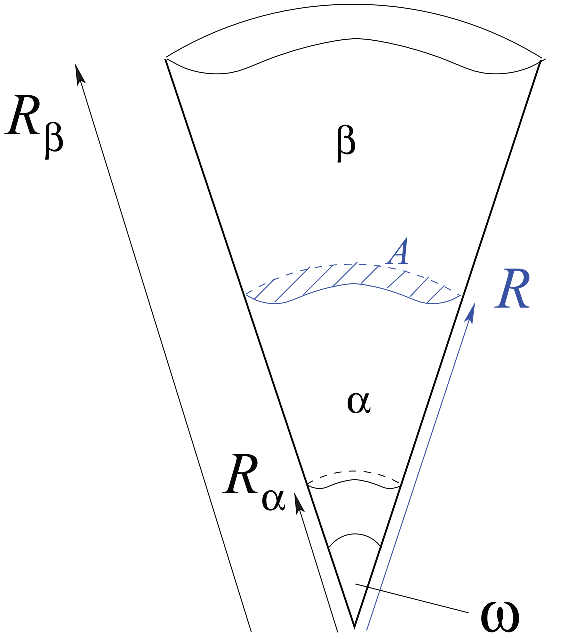

FIG. 1. Cone construction for the thermodynamic discussion of a spherical interface.

$$\Delta p := p_\alpha - p_\beta, \tag{7}$$

at coexistence will be different from zero. To exploit the scaling relations following from extensivity in the presence of a spherical interface, a clever cone construction[3,20,21,24] is considered, see Fig. 1. Here, both phases α, β reside in segments of a cone with opening solid angle ω, delimited by radii R_α, R (phase α) and R, R_β (phase β). Thus the corresponding volumes are $V_\alpha = \omega(R^3 - R_\alpha^3)$, $V_\beta = \omega(R_\beta^3 - R^3)$. R_α and R_β remain fixed, while the choice of the radius R of the Gibbs dividing surface $A = \omega R^2$ is at our disposal. Trading the set of parameters $(\omega, R_\alpha, R, R_\beta)$ for the physically more useful quantities $(V_\alpha, V_\beta, A, R)$, we write the differential of the total grand potential as

$$\begin{aligned} d\Omega = &-SdT - p_\alpha dV_\alpha - p_\beta dV_\beta \\ &+ \sigma dA + CdR - Nd\mu, \end{aligned} \tag{8}$$

where $p_\alpha = p_\alpha(T, \mu)$, $p_\alpha = p_\beta(T, \mu)$. The whole point of the cone construction is that it allows to exploit extensivity via scaling of the solid angle ω. Varying $\omega \to \lambda\omega$, the resulting Euler relation allows to integrate Eq. (8) as

$$\Omega = -p_\alpha V_\alpha - p_\beta V_\beta + \sigma A. \tag{9}$$

However, any dependence of a physical quantity like Ω on R introduced in this way is of course only superficial. To put this into mathematical terms, let $[d/dR]$ denote the so-called *superficial* or *notional derivative*[21] in which R is varied while keeping the physical state of the system invariant. Using this notation, $[d\Omega/dR] \equiv 0$ must vanish, which easily yields from Eq. (8) the *generalized Laplace equation*

$$\Delta p := p_\alpha - p_\beta = \frac{2\sigma}{R} + \frac{C}{A} \tag{10}$$

and a comparison of the notional derivative of (9) with that of the standard form $\Omega = \Omega(T, V_\alpha, V_\beta, A, R, \mu)$ in Eq. (8) allows to identify

$$C = A\left[\frac{d\sigma}{dR}\right]. \tag{11}$$

For the excess grand potential, we immediately deduce from Eq. (9) that the identification $\Omega^x = \sigma A$ of the surface tension with the excess grand potential per unit area (Eq. (6)) holds without change. Explicitly comparing the corresponding derivatives of Ω^x computed from the right hand side of Eq. (6) to those obtained using the integrated representation (9), it is easy to see that Ω^x is independent of V_α, V_β, and in addition σ is also independent of A, such that only the nontrivial dependencies

$$d\sigma = -s^x dT + c\,dR - \Gamma d\mu \tag{12}$$

remain, where we abbreviated

$$s^x := S^x/A, \quad c := C/A, \quad \Gamma := N^x/A. \tag{13}$$

In particular, the *adsorption* Γ will play a prominent role in what follows. Superficially, all quantities appearing in Eqs. (12) and (13) are thus functions of T, R, and μ. Physically, however, the parameters T, R, and μ are not independent. In fact, for a simple fluid the Gibbs phase rule predicts that only *one* intensive thermodynamic parameter can be independently varied at two-phase coexistence, but in presence of a spherical interface, the usual derivation of this rule no longer holds due to the breakdown of conventional extensivity. In fact, since for various interface curvatures different pressures $p_\alpha \neq p_\beta$ are possible for a whole range of temperatures T, we realize that phase coexistence involving curved interfaces of undetermined curvature allows for *two* independent parameters constructed from the above three. Usually, a grand canonical system at constant volume is described by the intensive parameters (T, μ), but since in the present context we are interested in understanding the curvature dependence of the interface tension, we intend to parametrize our system by (T, R). Generally, such a reparametrization can be realized by imposing a constraint of type $\gamma(T, R = R_\gamma, \mu) \equiv 0$, which amounts to *fixing the dividing surface to a value* $R = R_\gamma$. Conversely, we may regard this constraint as defining an implicit function $\mu = \mu(T, R_\gamma)$. Thus, if we impose the constraint

$$0 \equiv c(T, R_s, \mu), \tag{14}$$

which defines the so-called *surface of tension* with its associated radius R_s. Comparison with (12) yields

$$\left(\frac{\partial\sigma}{\partial R_s}\right)_T = -\Gamma\left(\frac{\partial\mu}{\partial R_s}\right)_T. \tag{15}$$

To compute the derivative $(\partial\mu/\partial R_s)_T$, one subtracts the Gibbs–Duhem relations pertaining to both bulk phases α, β, which yields at constant T,

$$0 = -d(\Delta p)|_T + \Delta\rho\, d\mu|_T, \tag{16}$$

where $\Delta\rho = \rho_\alpha - \rho_\beta$ denote the number density differences of the bulk phases. At constant T, a variation of Δp and $\Delta\mu$ only depends on a variation of R_s; therefore, we obtain

$$\Delta\rho\left(\frac{\partial\mu}{\partial R_s}\right)_T = \left(\frac{\partial\Delta p}{\partial R_s}\right)_T. \tag{17}$$

The constraint (14) is equivalent to the validity of the classical Laplace equation when used in Eq. (10),

$$\Delta p(T, R_s) = \frac{2\sigma(T, R_s)}{R_s}. \tag{18}$$

Thus, the remaining derivative on the right-hand side of Eq. (17) can now be calculated in terms of $\sigma(T, R_s)$ and $(\partial\sigma(T, R_s)/\partial R_s)_T$ after taking an isothermal derivative of Eq. (18). Inserting the result into Eq. (15), we obtain after some straightforward manipulations,

$$\left(\frac{\partial \ln\sigma}{\partial \ln R_s}\right)_T = \frac{2\Gamma_s}{R_s\Delta\rho}\left(1 + \frac{2\Gamma_s}{R_s\Delta\rho}\right)^{-1}, \tag{19}$$

where $\Gamma_s \equiv \Gamma(T, R_s)$ denoted the adsorption at the surface of tension. Using polar coordinates for our cone, Γ_s is readily computed as

$$\Gamma_s = \int_{R_\alpha}^{R_s} dr\frac{r^2}{R_s^2}(\rho(r) - \rho_\alpha) + \int_{R_s}^{R_\beta} dr\frac{r^2}{R_s^2}(\rho(r) - \rho_\beta). \tag{20}$$

On the other hand, at the radius R_e of the *equimolar surface*, the adsorption

$$\Gamma(T, R_e, \mu) \equiv 0 \tag{21}$$

vanishes by definition, such that

$$0 = \int_{R_\alpha}^{R_e} dr\frac{r^2}{R_s^2}(\rho(r) - \rho_\alpha) + \int_{R_e}^{R_\beta} dr\frac{r^2}{R_s^2}(\rho(r) - \rho_\beta). \tag{22}$$

Subtraction of both equations results in

$$\Gamma_s = \frac{\Delta\rho}{R_s^2}\int_{R_s}^{R_e} d^2r = \frac{\Delta\rho}{3R_s^2}\left(R_e^3 - R_s^3\right). \tag{23}$$

In terms of parameters (T, R_s), of course $R_e = R_e(T, R_s)$, and in terms of the famous *Tolman length*

$$\delta = \delta(T, R_s) := R_e(T, R_s) - R_s, \tag{24}$$

we arrive at

$$\frac{\Gamma_s}{\Delta\rho} = \delta\left[1 + \frac{\delta}{R_s} + \frac{1}{3}\left(\frac{\delta}{R_s}\right)^2\right]. \tag{25}$$

Altogether, this yields the desired isothermal R_s-dependence of the interface tension, encoded in the *Gibbs–Tolman–Koenig–Buff (GTKB) equation*

$$\left(\frac{\partial \ln\sigma}{\partial \ln R_s}\right)_T = \frac{\frac{2\delta}{R_s}\left[1 + \frac{\delta}{R_s} + \frac{1}{3}\left(\frac{\delta}{R_s}\right)^2\right]}{1 + \frac{2\delta}{R_s}\left[1 + \frac{\delta}{R_s} + \frac{1}{3}\left(\frac{\delta}{R_s}\right)^2\right]}. \tag{26}$$

In attempting to solve this equation, one should keep in mind that the Tolman length δ is expected to be a nontrivial function of R_s, in which case the GTKB equation is quite intractable.

Following the natural *ad hoc* conjecture of Tolman,[17] one usually makes the simple assumption that, at least for R_s large enough, $\delta(T, R_s) \approx \delta_\infty(T)$ saturates, i.e., becomes approximately independent of R_s, and hopes for the best. Since $\delta_\infty(T)$ is expected to be a quantity on the molecular scale, $\delta_\infty(T)/R_s$ should then be small, such that it suffices to keep powers of lowest order of this quantity on the right hand side of Eq. (26). Furthermore, for large R_s, the interface tension itself should also approach its limiting planar value $\sigma_\infty(T)$. Under these assumptions, Eq. (26) is readily integrated to give the well-known Tolman formula

$$\sigma_s \equiv \sigma(T, R_s) = \frac{\sigma_\infty(T)}{1 + 2\delta_\infty(T)/R_s} + O((\delta_\infty/R_s)^2) \quad (27)$$

and, replacing R_s by $R_s - \delta_\infty(T)$, to a similar level of accuracy also

$$\sigma_e \equiv \sigma(T, R_e) = \frac{\sigma_\infty(T)}{1 + 2\delta_\infty(T)/R_e} + O((\delta_\infty/R_e)^2). \quad (28)$$

In passing, we note that despite of contrary beliefs in the literature, the GTKB equation can then be solved analytically without any approximation beyond assuming $\delta_\infty(T)$ to be independent of R_s by the technique of partial fraction decomposition (see, e.g., Ref. 25 or Refs. 26–28). However, this is more of a mathematical exercise, since our simulation results below will show that the hypothesis that δ is independent of R_s must be abandoned, at least in the range of radii R_s that are physically relevant for real-world thermodynamics. In contrast, one can prove that the remarkable identity[20]

$$\left(\frac{\partial \ln \sigma_e}{\partial \ln R_e}\right)_T = \left(\frac{\partial \ln \sigma_s}{\partial \ln R_s}\right)_T \quad (29)$$

holds *exactly*, i.e., without any assumption on the R_s-dependence of the Tolman length made. Also, from Eqs. (12) and (21), we conclude that

$$\left(\frac{\partial \sigma_e}{\partial R_e}\right)_T = c = \left[\frac{d\sigma}{dR}\right]_{R=R_e}, \quad (30)$$

i.e., if (and only if) R_e is chosen as our radial parameter, the notional and isothermal derivative of the interface tension coincide. These formulas might suggest that a parametrization of the system by R_e is just as convenient as by R_s, and of course both quantities encode the same physical information. However, R_s plays a distinguished role among all possible choices of radii. The reasons for this are at least twofold. On the one hand, eliminating Δp between Eqs. (18) and (10) and solving the resulting ordinary (notional) differential equation for $\sigma(T, R)$ yields the universal parametrization

$$\frac{\sigma(R)}{\sigma_s} = 1 + \frac{1}{3}\left(\frac{R - R_s}{R}\right)^2 \frac{(R_s + 2R)}{R_s}. \quad (31)$$

In other words, knowledge of R_s and σ_s suffices to immediately deduce σ for any other notional variation of R, and in particular, R_s locates the *minimum value* σ_s of $\sigma(R)$ under all such variations. On the other hand, an easy calculation shows that the formation free energy barrier $\Delta\Omega$ for a spherical droplet is

$$\Delta\Omega = \frac{4\pi R^2}{3}\left(\sigma - R\left[\frac{d\sigma}{dR}\right]\right). \quad (32)$$

Of course, this quantity is independent of the particular choice of R, but the simple relation

$$\Delta\Omega(T, R_s) = \frac{4\pi R_s^2}{3}\sigma(T, R_s), \quad (33)$$

used in classical nucleation theory is only recovered if the surface of tension is chosen as the dividing surface.[3,4]

III. FREE-ENERGY-BASED NUMERICAL APPROACHES TO DETERMINE σ AND δ

We now explain how to fit the above concepts in the framework of a simulation study of droplets in finite box volumes (see, e.g., Ref. 9 for details). Consider, say, a one-component fluid in a cubic box of size $V = L^d$ with periodic boundary conditions. For a fixed temperature T well below the critical point temperature T_c, we determine the gross features of probability distribution $P_{TV\mu}(N)$. This quantity is rigorously definable, but in practice will only be obtained numerically by, e.g., conducting a grand-canonical Monte Carlo simulation. For a certain narrow range of values μ, the single Gaussian-like shape of $P_{TV\mu}(N)$ changes to a double-peak structure which signals the two-phase coexistence region. To minimize finite size corrections, one can fine-tune the coexistence chemical potential to the value $\mu = \mu_0(T)$ prescribed by the equal–weight rule[29] applied to these peaks (see the discussion below) using the well-known histogram re-weighting machinery.[30] Once $\mu_0(T)$ has been determined and fixed, the fine-structure of $P_{TV\mu_0}(N)$ at $\mu = \mu_0(T)$ is resolved by flat histogram type sampling methods, e.g., successive umbrella sampling.[31] Taking its logarithm yields, the Helmholtz free energy

$$F(T, V, N) = F_0(T, V) + \mu_0(T)N + \hat{F}(T, V, N), \quad (34)$$

where

$$\hat{F}(T, V, N) = -k_B T \ln P_{TV\mu_0}(N), \quad (35)$$

and the function $F_0(T, V)$, which is related to the choice of normalization of $P_{TV\mu_0}(N)$, will be unimportant for what follows. From the double-peak shape of $\ln P_{TV\mu_0}(N)$, $\hat{F}(T, V, N)$ inherits the appearance of a double-well, whose minima at $N_g = V\rho_g$, $N_l = V\rho_l$, which correspond to the equilibrium densities of the coexisting gas and liquid phases, are separated by a free energy barrier of height $\propto L^2$, which displays a central plateau and fine additional features to the left and the right of this plateau which are related to the different geometries of phase-separated configurations. In all cases known to the authors, the free energy values of both minima of $\hat{F}(T, V, N)$ seem to roughly agree within the accuracy of the simulations. While this is to be expected for models, for which the coexisting phases are symmetry-related (e.g., in Ising/lattice gas systems), this seems to be purely coincidental in general. In fact, the widths of the corresponding two quasi-Gaussian peaks in $P_{TV\mu_0}(N)$ are controlled by $1/V\rho^2\kappa_T$, and these numbers are not equal in general when being evaluated for the phases α and β, respectively. Thus, if we impose equal weight,[29] the heights of the two peaks should necessarily be different.

Taking the derivative $(\partial/\partial N)_{T,V}$ of Eq. (34), we obtain the *canonical* chemical potential $\mu(T, V, N)$. Could we invoke the thermodynamic limit, then $\mu(T, V, N)$ would be classified as an intensive variable, and standard scaling arguments would allow to write its functional form as $\mu = \mu(T, \rho)$. In view of this notation, we choose to write $\mu = \mu_L(T, \rho)$ to indicate a possible finite size dependence of μ. A similar notation will also be used below for other "quasi-intensive" variables, such that, e.g., $F_L(T, V, N) \equiv V f_L(T, \rho)$. Using this notation, we can split

$$\mu_L(T,\rho) = \mu_\infty(T) + \hat{\mu}_L(T,\rho), \tag{36}$$

where (in an abuse of language) the canonical "excess chemical potential" $\hat{\mu}_L$ is

$$\hat{\mu}_L(T,\rho) = \left(\frac{\partial \hat{f}_L(T,\rho)}{\partial \rho}\right)_T, \tag{37}$$

and we have passed to volume densities. Globally, $\hat{\mu}_L(T, \rho)$ appears to have the shape of a distorted "van der Waals loop" (Fig. 3). As can be anticipated from the shape of $\hat{F}$, we find a constant central plateau of value zero, a sharp maximum at some density $\rho_{\max}$ smaller than the plateau range but slightly larger than ρ_g, and a sharp minimum at a density $\rho_{\min}$ than the plateau range but somewhat smaller than ρ_l. Thus, for any prescribed "unsaturated" value μ within the range $\mu_\infty(T) + \hat{\mu}_L(T, \rho_{\min}) < \mu < \mu_\infty(T) + \hat{\mu}_L(T, \rho_{\max})$, the equation $\mu_L(T, \rho) \equiv \mu$ generally has (at least) three roots $\rho_\alpha(T, \mu) < \rho(T, \mu) < \rho_\beta(T, \mu)$. By calling on the identity of chemical potentials at phase coexistence, we interpret these densities as the bulk densities of coexisting phases. The values of the corresponding grand potential densities corresponding to the states of the total system and of the bulk states characterizing the coexisting subsystems α, β are

$$\omega(T,\mu) = f_L(T,\rho(T,\mu)) - \mu_L \rho(T,\mu), \tag{38}$$

$$\omega_\alpha(T,\mu) = f_L(T,\rho_\alpha(T,\mu)) - \mu_L \rho_\alpha(T,\mu), \tag{39}$$

$$\omega_\beta(T,\mu) = f_L(T,\rho_\beta(T,\mu)) - \mu_L \rho_\beta(T,\mu), \tag{40}$$

where the use of the Legendre transform for our necessarily finite systems is admittedly delicate. Inspection of Figs. 2 and 3 suggests, however, that for the parts of the data that correspond to pure phases finite size effects are not significant. Inserting $\mu_L = \mu_\infty + \hat{\mu}_L$ and using Eq. (34), this reads

$$\omega(T,\mu) = f_\infty(T) + \hat{f}_L(T,\rho(T,\mu)) - \hat{\mu}_L \rho(T,\mu), \tag{41}$$

$$\omega_\alpha(T,\mu) = f_\infty(T) + \hat{f}_L(T,\rho_\alpha(T,\mu)) - \hat{\mu}_L \rho_\alpha(T,\mu), \tag{42}$$

$$\omega_\beta(T,\mu) = f_\infty(T) + \hat{f}_L(T,\rho_\beta(T,\mu)) - \hat{\mu}_L \rho_\beta(T,\mu). \tag{43}$$

Thus, after transforming to the free energy densities $\hat{f}$ the homogeneous background part μ_∞ drops out from the calculations.

The interface tension corresponding to a partition $V = V_\alpha + V_\beta$ with dividing surface A is

$$\sigma_L = \frac{\hat{F}_L^x - \hat{\mu}_L N^x}{A}, \tag{44}$$

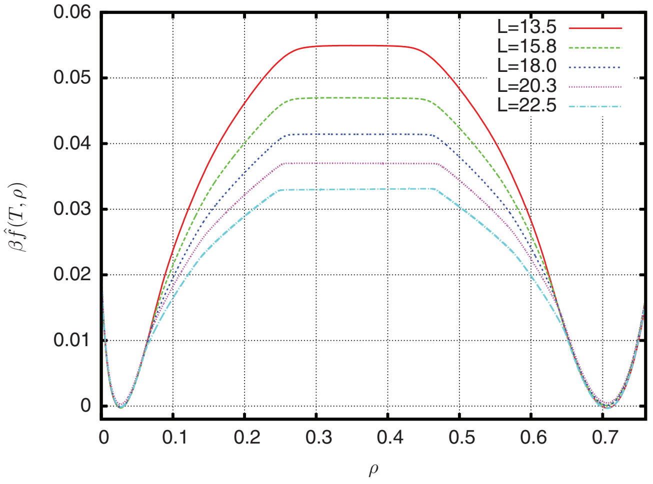

FIG. 2. Dimensionless free energy densities $\beta\hat{f}(T,\rho)$ for truncated Lennard–Jones potential at temperature $T = 0.78 \cdot T_c$ for linear sizes $L = 13.5, 15.8, 18.0, 20.3, 22.5$.

at common $\hat{\mu} = \hat{\mu}(T, \rho)$, with excess contributions

$$\hat{F}_L^x = V\hat{f}_L(T,\rho(T,\hat{\mu})) - V_\alpha f_L(T,\rho_\alpha(T,\hat{\mu})) - V_\beta f_L(T,\rho_\beta(T,\hat{\mu})), \tag{45}$$

$$N^x = V\rho(T,\hat{\mu}) - V_\alpha\rho_\alpha(T,\hat{\mu}) - V_\beta\rho_\beta(T,\hat{\mu}). \tag{46}$$

Formula (44) gives the interface tension at arbitrary R. According to the theory developed in Sec. II, it is therefore straightforward to determine the radius R_s and the corresponding interface tension $\sigma(R_s)$ by numerically locating the minimum of this function. On the other hand, by plugging the three roots $\rho_\alpha < \rho < \rho_\beta$ into the lever rule

$$\frac{V_\alpha}{V} = \frac{\rho - \rho_\beta}{\rho_\alpha - \rho_\beta}, \quad \frac{V_\beta}{V} = \frac{\rho_\alpha - \rho}{\rho_\alpha - \rho_\beta}, \tag{47}$$

it is also easy to calculate R_e and evaluate $\sigma(R)$ at this radius.

After completing these steps, we are in possession of the radii R_s, R_s and the corresponding interface tensions σ_s and

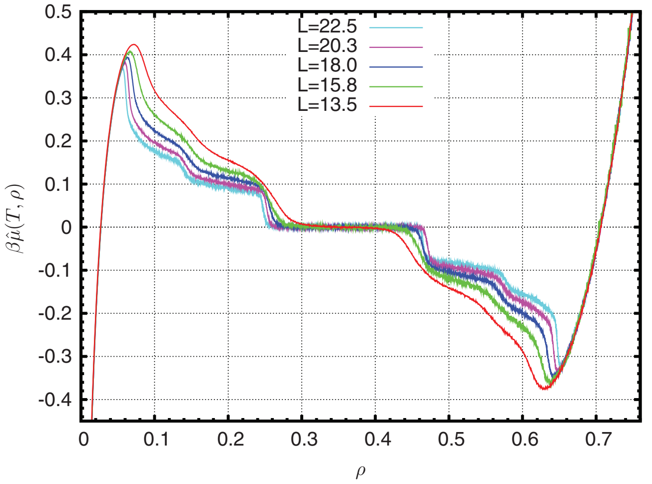

FIG. 3. Dimensionless canonical chemical excess potentials $\beta\hat{\mu}_L(T,\rho)$ for truncated Lennard–Jones potential at temperature $T = 0.78 \cdot T_c$ for linear sizes $L = 13.5, 15.8, 18.0, 20.3, 22.5$.

σ_e. Thus, the Tolman length $\delta(T, R_s)$ can in principle immediately be determined using its very definition (24). Note that the present procedure does not make any use of the simple Tolman formula (27), and neither any further approximations nor any optimistic assumptions on the corresponding behavior of δ as a function of R_s are needed.

Of course, one may also compare the results of such a procedure to alternative numerical strategies. For instance, from the data of simulations as outlined above, it is also straightforward to calculate the adsorption Γ_s at the surface of tension. Thus, with the left hand side and the value of R_s known, Eq. (25) represents a cubic equation for $\delta(T, R_s)$, whose single real-valued solution is obtained from standard formulas. Ultimately, one is mainly interested in the behavior of $\delta(R_s)$ in the limit $R_s \to \infty$, for which formula (25) reduces to[18]

$$\delta(T, R_s) \approx \frac{\Gamma_s}{\Delta\rho} \quad \text{for } \delta(T, R_s)/R_s \ll 1. \tag{48}$$

Comparing the case of spherical liquid droplets in a vapor environment to the inverse one of spherical bubble cavities in a liquid, we expect the respective adsorptions Γ_s to approach a common value $\Gamma_s(R_s = \infty)$ in the limit of a planar interface. On the other hand, in this limit the relative density differences $\Delta\rho$ should approach a common modulus but, of course, have opposing sign from the droplet and bubble perspective, respectively. The limiting Tolman lengths $\delta = \delta(R_s = \infty)$ obtained for droplets and bubbles should thus be identical up to sign, which conforms to a naive replacement $R_s \to -R_s$ in the simple Tolman formula (27). In passing, we note that this immediately implies that for any system, in which the two coexisting phases are related by symmetry (e.g., an Ising lattice gas) the Tolman length $\delta_\infty(T)$ necessarily vanishes.[32]

In the literature,[33] the numerical strategy implied by Eqs. (25) and (48) has been termed the *direct route* to δ. On the other hand, from Eq. (12), we instantly get

$$-\frac{1}{\Delta\rho}\left(\frac{\partial\sigma}{\partial\hat{\mu}}\right)_T = \frac{\Gamma_s}{\Delta\rho} \tag{49}$$

If we again regard the excess chemical potential $\hat{\mu}$, which characterizes the over-saturation of the metastable phase, as a function of R_s, i.e.,

$$\mu = \mu_{\mathrm{coex}}(T) + \hat{\mu}(T, R_s), \tag{50}$$

then sending $R_s \to \infty$ amounts to extrapolating $\hat{\mu} \to 0$. While mathematically in full equivalence with other approaches, Koga *et al.*[33] claim that this method to obtain $\delta_\infty(T)$, which they term the *adsorption route*, has certain numerical advantages. Explicitly, $\delta_\infty(T)$ is then determined from the relation

$$\delta_\infty(T) = -\lim_{\hat{\mu}\to 0} \frac{1}{\Delta\rho(\hat{\mu})}\left(\frac{\partial\sigma(\hat{\mu})}{\partial\hat{\mu}}\right)_T, \tag{51}$$

in which $1/\Delta\rho(\hat{\mu})$ generally depends only weakly on $\hat{\mu}$. The derivative $(\partial\sigma(R_s)/\partial\hat{\mu}(R_s))_T$ must be evaluated by numerical differentiation. In this context, we note that in Ref. 34, a linear relation between $\delta(R_s)$ and $\hat{\mu}$ is observed in a seemingly phenomenological way and is utilized for extrapolating $\delta(R_s)$ to $R_s \to \infty$.

In closing this section, we nevertheless have to emphasize once more that trying to find the limiting value $\delta_\infty(T)$ will turn out to be a rather academic problem since $\delta(T, R_s)$ will be found to have saturated near such a limit only for values of R_s and accompanying free energy barriers that are so large that they are already irrelevant for any conceivable practical purpose, e.g., nucleation theory.

IV. SIMULATIONS

We now move on to breath live into the above ideas by using them to analyze previously obtained data for a 3d Lennard–Jones system of linear sizes $L = 13.5$, 15.8, 18.0, 20.3, 22.5, truncated and shifted to zero at $r = 2 \cdot 2^{1/6}\sigma$, where we have chosen Lennard–Jones units (see Ref. 35 for details). As explained above, the coexistence chemical potential μ_0 was determined by the equal area rule, and subsequently the dimensionless free energy densities $\beta\hat{f}(T, \rho)$ were determined at a temperature $T = 0.78T_c$ (cf. Fig. 2) from successive umbrella sampling simulations,[31] where $T_c \approx 0.999$ in the chosen units. Numerically differentiating $\beta\hat{f}_L(T, \rho)$, we then obtain $\hat{\mu}_L(T, \rho)$ (cf. Fig. 3).

Guided by the analysis of snapshots of typical configurations appearing in the simulations and visual inspection of the fine details of the main plot of Fig. 3, it is in principle possible to roughly locate for each linear size L the density ranges within which predominantly a—on average—spherical phase separation pattern (i.e., a liquid droplet or a vapor bubble) appears. However, proceeding in this way we would have to live with the accompanying uncertainties. In view of the delicate numerical problems to identify the fine details of the interface tension, in which any Tolman correction is buried, such an approach is therefore suboptimal. Instead, in the subsequent analysis we propose to consider provisional density regions which are chosen according to the less restrictive condition that they should only be chosen large enough to safely enclose the ones predominantly inhabited by spherically shaped clusters, postponing a strict determination of the spherical density domains to later stages of the analysis. In fact, if we impose the hypothesis of spherically shaped phase separation patterns on the data, we can anticipate that some observables computed from this analysis for different system sizes L may show systematic deviations from a common "master curve," from which we will be able to reliably identify the actual density regions for droplets and bubbles *a posteriori*. In addition, it turns out that in this way it is somewhat easier to observe certain systematic trends in the data.

The provisional density regions are depicted in Fig. 4, together with the sections of $\beta\hat{\mu}_L(T, \rho)$ corresponding to the completely homogeneous vapor and liquid states.

Within these density ranges, one may fit both $\beta\hat{f}_L(T, \rho)$ and $\beta\hat{\mu}_L(T, \rho)$ to suitable smooth functions. For prescribed total ρ, one then solves the equation $\beta\hat{\mu}_L(T, \rho) \equiv \beta\hat{\mu}_L(T, \rho_i)$ numerically for the coexistence densities ρ_i, $i = \alpha, \beta$ (see Fig. 5 for an illustration).

Evaluating the free energy density for such a triplet $(\rho_\alpha, \rho, \rho_\beta)$, we obtain a corresponding free energy density triplet $\beta\hat{f}_{L\mathrm{tot}} \equiv (\beta\hat{f}_L(T, \rho), \beta\hat{f}_{L\alpha} \equiv \beta\hat{f}_L(T, \rho),$ and $\beta\hat{f}_{L\beta}$

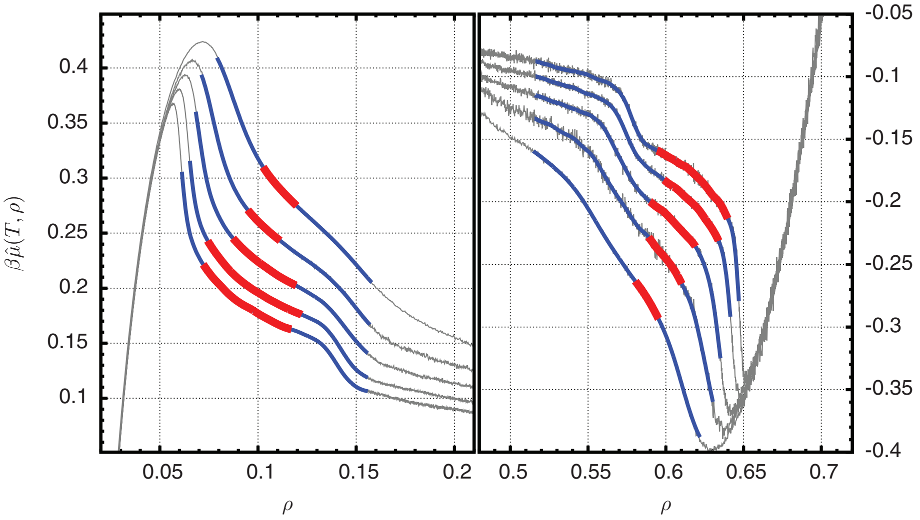

FIG. 4. Indication of provisional (blue) density ranges considered in our general analysis (cf. Table I), which enclose the resulting approximate actual (red) ones, for which predominantly roughly spherical liquid droplet (left plot) and vapor bubble (right plot) shapes are observed as typical microstates (cf. Table III below).

$\equiv f_L(T, \rho_\beta)$). Comparison to Eqs. (44) and (46) shows that we now possess all the ingredients necessary to compute the excess free energy density and number density, and thus the interface tension. In what follows, we will frequently suppress reference to the temperature T to lighten our notation. Figure 6 shows the typical behavior of $\sigma_L(R;\,\rho)$ as observed in numerically evaluating our simulation data. Given the function $\sigma_L(R;\,\rho)$ is straightforward to determine its minimum, such that we obtain the desired quantities R_s and $\sigma_s^{(L)} \equiv \sigma_L(R_s;\rho)$ for each given triple of densities $(\rho_\alpha,\,\rho,\,\rho_\beta)$ (we choose to suppress also the L-dependence of R_s and R_s to lighten our notation). In passing, we note that once R_s and $\sigma_s^{(L)}$ have been determined, the correctness of the whole procedure can conveniently be checked by comparing the observed R-dependence of Eq. (44) with the universal form of Eq. (31).

In addition to R_s, the equimolar radius R_e can also readily be computed using Eq. (47). In accordance with the above condensed notation, we will denote the corresponding surface tension at the equimolar surface as $\sigma_e^{(L)} \equiv \sigma_L(R_e;\rho)$. Information on the planar interface tension $\sigma_\infty^{(L)} = \sigma_L(R_s = \infty, \rho)$ is also available. One can measure the (average) free energy difference $\Delta\hat{F}_L$ between the central plateau value of the free energy and the value at one of the minima at ρ_α, ρ_β, which gives rise to the finite size planar interface tension estimator

$$\sigma_\infty^{(L)} = \frac{\Delta\hat{F}_L}{2L^{d-1}} = L\Delta\hat{f}_L/2. \tag{52}$$

By extrapolation of these finite size values to the thermodynamic limit, the planar interface tension σ_∞ at $T = 0.78\,T_c$

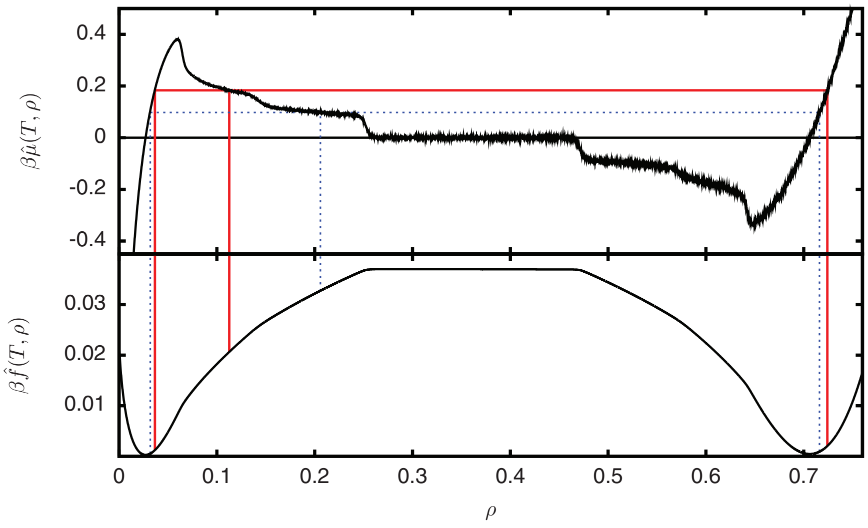

FIG. 5. Illustration of the numerical procedure to determine coexistence density triplets $(\rho_\alpha,\,\rho,\,\rho_\beta)$ for $L = 20.3$. Full red lines indicate an example solution $(\rho_\alpha,\,\rho,\,\rho_\beta) = (0.0366, 0.1126, 0.7241)$ at common chemical potential $\hat{\mu} = 0.18352$ corresponding to a spherical droplet, while dotted blue lines refer to an example solution $(\rho_\alpha,\,\rho,\,\rho_\beta) = (0.0319, 0.2059, 0.7161)$ at common chemical potential $\hat{\mu} = 0.0977$ characterizing a cylindrical droplet.

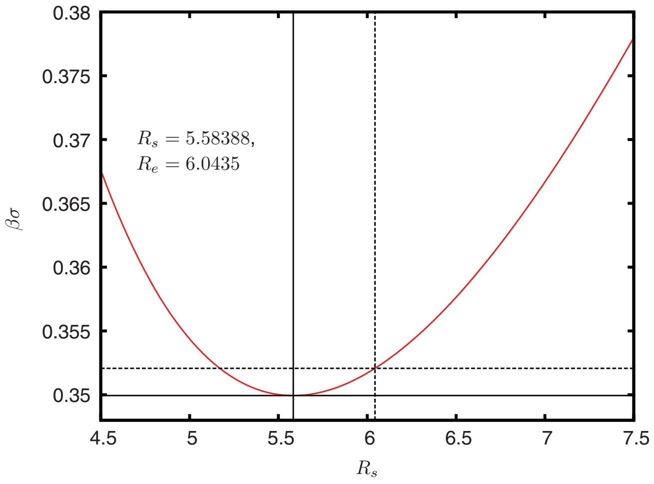

FIG. 6. $\beta\sigma_L(R;\rho)$ for $L = 20.3$ as computed for the spherical example density triplet of Fig. 5. $R = R_s$ coincides with the location of the minimum with value $\beta\sigma_s^{(L)}$, while the auxiliary lines denote the radius of the equimolar surface $R = R_e$ as calculated from the lever rule (47) and the corresponding equimolar surface tension $\beta\sigma_e^{(L)}$, respectively.

TABLE I. Preliminary density ranges chosen by visual inspection of the main plot of Fig. 3 to enclose the density ranges in which roughly spherical liquid droplet/vapor bubble shapes dominate in the typical microscopic system configurations observed for the systems sizes L considered.

L	Low density range	High density range
13.5	0.079−0.158	0.5147−0.6221
15.8	0.071−0.157	0.5155−0.6304
18.0	0.068−0.156	0.5159−0.6353
20.3	0.065−0.156	0.5161−0.6417
22.5	0.061−0.156	0.5161−0.6470

was estimated in Ref. 35 as $\beta\sigma_\infty \approx 0.375$. With (27) in mind, this value serves as a natural normalization of $\sigma_s^{(L)}$ and $\sigma_e^{(L)}$.

As Fig. 7 shows, the resulting values of $\sigma_s^{(L)}$ collected from our simulation results at system sizes L = 13.5, 15.8, 18.0, 20.3, 22.5 appear to roughly collapse onto two separate families of curves for liquid droplets and vapor bubbles, respectively, which are slightly but systematically offset from one another. The fact that these offsets decay systematically between neighboring systems of increasing size indicates that these offsets represent a finite size effect. A discussion of possible origins of these finite size deviations, which may not have been expected to be so large at a first order transitions is postponed until the closing discussion of the paper. The data show, of course, a pronounced R_s-dependence over the whole range of observed radii. However, as anticipated, above, due to the generous choice of density ranges summarized in Table I, sections of the data this R_s-dependence is physically irrelevant, as it merely represents the crossover from spherical to cylindrically phase-separated as well as homogeneous system configurations which we implicitly ignored in our evaluation. Unfortunately, however, from these interface tension data alone it is clearly very difficult to get an idea of the exact locations of these crossover regions. Thus, let us postpone this question for a moment and turn directly to the data for $\delta(R_s)$ instead.

Figure 8 shows a plot of the corresponding data of $\delta(R_s) = R_e - R_s$ as calculated from our simulation and plotted against $1/R_s$, which is suitable for studying the behavior for growing R_s. Looking at these curves, one notices the onset of an only weakly L-independent linear segment in the both the droplet as well as the bubble data for values around 0.15–0.25 in $1/R_s$. The boundary values for these segments depend on the system size L. We can determine them by fitting straight lines to the data and locating the approximate boundary values for which these fits begin to break down by visual inspection (cf. Fig. 8). As each value of R_s is in one-to-one correspondence with a total system density ρ, these results, which are gathered in Table II, immediately translate into the density ranges listed in Table III.

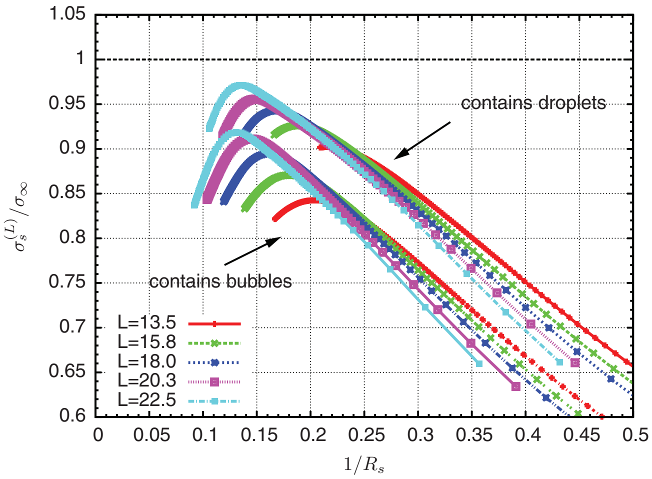

FIG. 7. Provisional results for the reduced spherical interface tension $\sigma_s^{(L)}/\sigma_\infty$ for system sizes L = 13.5, 15.8, 18.0, 20.3, 22.5 using the provisional density ranges of Table I. The upper branches of data contain parts corresponding to configurations with a liquid droplet, while the lower ones have parts which characterize vapor bubbles inside a liquid environment, respectively.

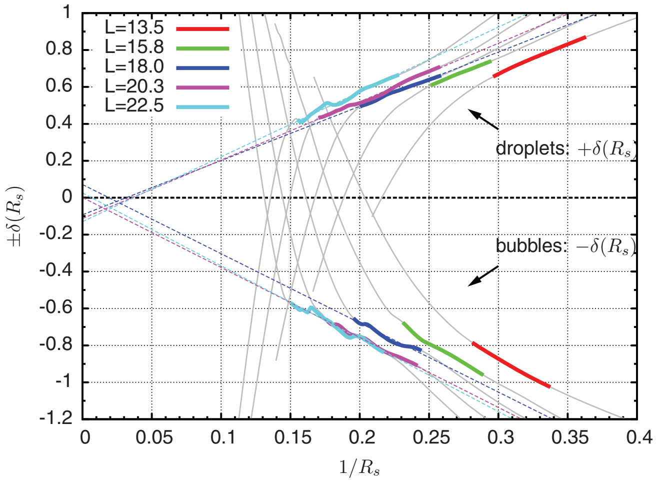

FIG. 8. Grey lines show the behavior of $\pm\delta(R_s)$ against $1/R_s$ obtained for system sizes L = 13.5, 15.8, 18.0, 20.3, 22.5 based on the preliminary density ranges of Table I. In colored thick lines, approximately linear segments of these $\pm\delta(R_s)$ curves are shown, with corresponding linear fits for the three largest system sizes L = 18.0, 20.3, 22.5.

TABLE II. Approximate R_s^{-1}-values confining the linear segments observed in $\delta(R_s)$.

L	Droplet inverse radii	Bubble inverse radii
13.5	0.295–0.365	0.280–0.340
15.8	0.250–0.295	0.230–0.290
18.0	0.200–0.260	0.195–0.245
20.3	0.170–0.260	0.175–0.245
22.5	0.155–0.230	0.150–0.220

Visually inspecting these density ranges, which are indicated in Fig. 4, we realize that they are in excellent correspondence with our expectations concerning the density domains for which roughly spherical liquid droplet/vapor bubble shapes are observed dominate in the typical microscopic system configurations when taking snapshots of the system configurations during the course of the simulation.

From the theorist's point of view as well as from a DFT perspective, the above observations may be appreciated. In fact, there are theoretical arguments[36,37] predicting the Tolman length to have an asymptotic behavior of the form

$$\delta(R_s) \sim \delta_\infty + \text{const.}/R_s, \qquad R_s \to \infty, \tag{53}$$

which also supports our interpretation. Below we will show in addition that the observed linear behavior of the Tolman length with respect to $1/R_s$ is also in excellent qualitative agreement with results from density functional theory.

Having successfully determined the density and radial ranges that are actually populated by spherical droplets and bubbles, we return to the analysis of the interface tension data. Within as well as outside of the spherical segments, the data of Fig. 9 exhibit a pronounced R_s-dependence. In particular, the droplet interface tension seem to suggest a certain "overshooting" of $\sigma_s^{(L)}$ to values larger than σ_∞. In terms of the simple Tolman formula (27), one would be tempted to propose a negative Tolman length, which could be obtained from a corresponding fit.[35] Nevertheless, in the light of the data on $\delta(R_s)$ presented above, this conclusion resides on shaky ground, as large enough radii R_s for which $\delta(R_s)$ is close to an asymptotic value have not been reached remotely for the data at hand. In any case, merely replacing $\sigma_s^{(L)}$ by σ_∞, as it is done in the capillarity approximation, can yield large errors in derived quantities. In particular, this warning applies to the determination of nucleation rates, in which the third power of the interface tension enters exponentially. To illustrate the magnitude of potential errors, Fig. 10 shows a comparison of estimates of the pressure difference Δp_L inside and outside a liquid droplet computed from the Laplace equation as opposed to the simple capillarity approximation $\Delta p \approx 2\sigma_\infty/R$.

TABLE III. Density ranges corresponding to the inverse radius ranges of Table II.

L	Droplet densities	Bubble densities
13.5	0.102–0.119	0.580–0.595
15.8	0.094–0.111	0.588–0.610
18.0	0.086–0.119	0.589–0.619
20.3	0.074–0.122	0.589–0.634
22.5	0.071–0.117	0.594–0.639

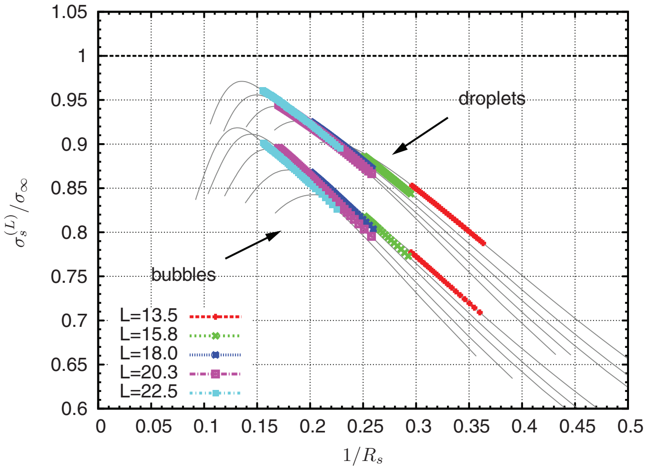

FIG. 9. Results for the reduced spherical interface tension $\sigma_s^{(L)}/\sigma_\infty$ for system sizes $L = 13.5, 15.8, 18.0, 20.3, 22.5$ using the inverse radius ranges of Table II. The upper branches of the data correspond to configurations with a liquid droplet, while the lower ones refer to a spherical vapor bubbles inside a liquid environment, respectively.

Summarizing our results so far, within the observed range of radii and system sizes, $\delta(R_s)$ is strongly R_s dependent with a behavior following Eq. (53), and from a purely *mathematical* point of view it is obvious that at radii R_s much larger than those accessible in our simulations $\delta(R_s)$ finally saturates and Tolman's formula becomes correct. However, as we now show, our simulations do cover the *physically* relevant range of radii R_s. To show this, we investigate the free energy barrier (33) for the formation of droplets and bubbles, respectively, which is a quantity of great interest in its own right, since it plays a major role into practically all experimental and theoretical approaches to nucleation problems. As Fig. 11 demonstrates, at the chosen temperature the corresponding barrier data $\Delta\Omega^{(L)}(R_s) = (4\pi/3)R_s^2\sigma_s^{(L)}$ computed

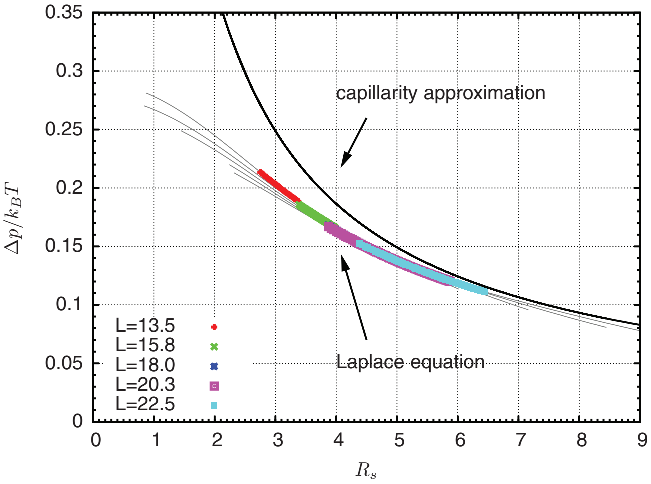

FIG. 10. Comparison of results for $\beta\Delta p_L$ computed from the Laplace equation (lower data) as opposed to the simple capillarity approximation $\Delta p \approx 2\sigma_\infty/R$ (upper data). Depending on the value of R_s, the error introduced by the capillarity approximation falls in the range of 10%–30%.

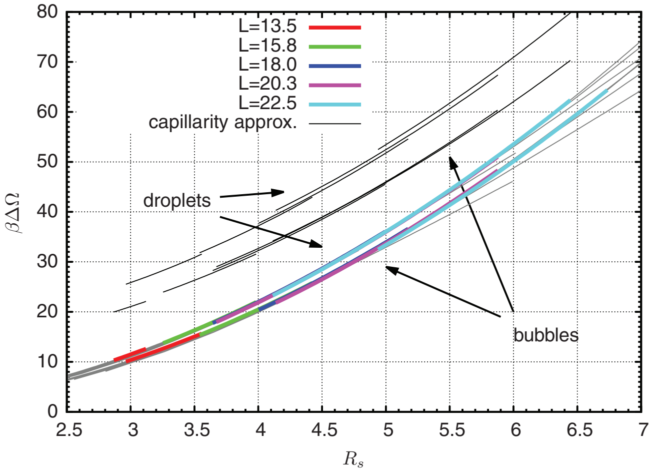

FIG. 11. Dimensionless formation free energy barriers obtained for the radii R_s accessed in our simulations. The overestimations introduced by the capillarity approximation are also indicated.

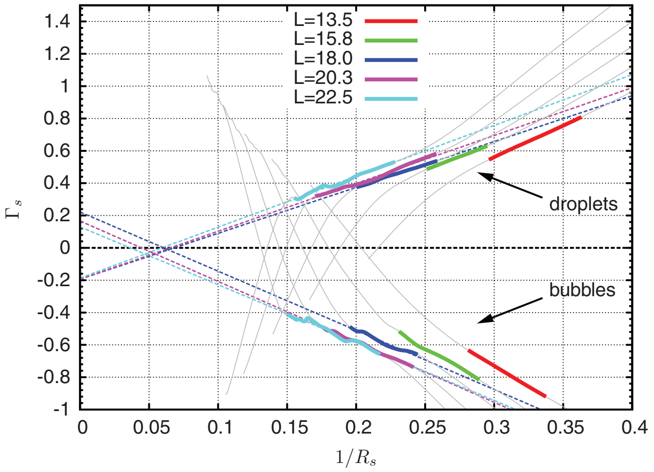

FIG. 12. Grey lines show the behavior of the adsorption Γ_s at surface of tension plotted as function of $1/R_s$. In colored thick lines, approximately linear segments of these Γ_s curves are shown, with corresponding linear fits for the three largest system sizes $L = 18.0$, 20.3, 22.5.

with the aid of Eq. (33) exceed some $65k_BT$ for system sizes beyond those considered here. Barriers in this range are certainly of practical interest, while significantly larger barriers would not matter for observable nucleation rates at all.

Another important lesson that Fig. 11 teaches us is how important it is to use the proper definition of surface tension and droplet radius when one wishes to employ the classical formula, Eq. (33), according to which the barrier is just 1/3 of the total surface free energy of the droplet. In fact, the spherically relevant part of a mere *graph* of $\sigma(R_e)$ plotted against R_e may appear to be deceivingly similar to that of σ_s plotted against R_s, since Eq. (6) illustrates that accidentally the larger value $\sigma_e > \sigma_s$ is also taken at a larger radius $R_e > R_s$ for our present model. Nevertheless, the classical formula, Eq. (33), only applies if R is taken to be the radius of surface of tension R_s and σ as the associate interface tension σ_s, whereas it would be rather inaccurate to use the equimolar radius and associate surface free energy instead. This fact can be easily illustrated with the data shown in Fig. 6 for a chosen chemical potential difference $\widehat{\mu} \approx 0.183$: the radius $R_s = 5.583$ and dimensionless surface tension $\beta\sigma = 0.350$ translate into a barrier (in units of k_BT) of 46.2, while the radius $R_e = 6.0435$ and dimensionless surface tension $\beta\sigma = 0.352$ yield the significantly larger value of about 54.3. In passing, we note that in Ref. 35, results similar to Figs. 9 and 11 were presented for the reduced interface tension at $R = R_e$ (cf. Fig. 6). However, the latter result is not directly relevant for nucleation theory, unlike the results shown in Fig. 9. With regard to the practical problem of determining nucleation barriers, we therefore consider the present treatment much more satisfactory.

One may also wonder how large the error introduced by a simple capillarity approximation $\sigma(R_s) \approx \sigma_\infty$ in computing the barrier $\Delta\Omega$ actually is. Eliminating R_s in Eq. (33) in favor of σ_s by virtue of the Laplace equation (18), the barrier is seen to depend cubically on σ_s. Thus, replacing $\sigma_s \approx \sigma_\infty$ leads to an overestimation of the barrier by the cubic factor $(\sigma_\infty/\sigma_s)^3$. As can be anticipated from a glance at Fig. 9, for the data at hand this overestimation, which is included in Fig. 11, is absolutely dramatic.

Returning to the analysis of $\delta(R_s)$, let us investigate our data for the adsorption Γ_s at the surface of tension. As Eq. (48) indicates, the question whether δ vanishes or not boils down to the question if Γ_s does so, since by physical reasons $\Delta\rho$ is generally expected to gently saturate at a finite and nonzero value in the limit of infinitely large "droplets" or "bubbles". Looking at Fig. 12, one notices once more the onset of an only weakly L-independent linear segment in the both the droplet as well as the bubble data for values of $1/R_s$ which are practically identical to those already determined above (Fig. 12). In addition, restricting the data to these ranges, our anticipation concerning the gentle variation of $\Delta\rho^{(L)}(R_s)$ in the limit $R_s \to \infty$ is confirmed, and, as Fig. 13 shows, the extrapolation of these data to $R_s \to \infty$ is compatible with the finite size extrapolation of the (practically L-independent) density difference $\Delta\rho^{(L)} = \rho_l - \rho_g$ formed by the two isolated zeros of $\hat{\mu}(T, \rho)$, which is estimated numerically as $\Delta\rho = \lim_{L\to\infty}\Delta\rho^{(L)} \approx 0.6796$ for our present model. As may have been expected

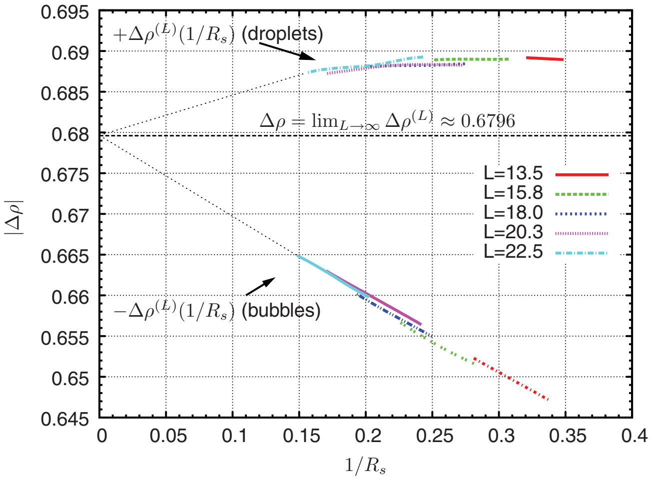

FIG. 13. Plot of $\pm\Delta\rho$ obtained for system sizes $L = 13.5$, 15.8, 18.0, 20.3, 22.5 for spherical liquid droplets and bubbles, respectively (the dotted lines are a guide to the eye).

on general grounds, a plot of the solution of Eq. (25) in an attempt to follow the "direct route to δ" gives results which are indistinguishable from the ones shown in Fig. 8. We have also tested the "adsorption route" to $\delta(R_s)$ outlined above. For the presently available set of data a corresponding analysis did not yield any significant improvement.

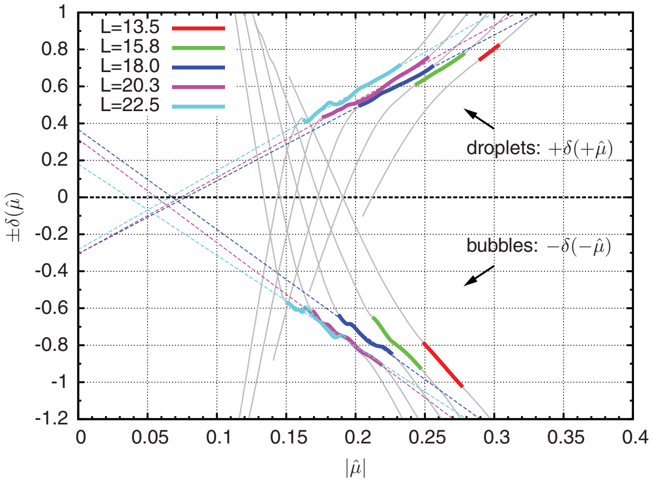

FIG. 14. Plot of $\pm\delta(\hat{\mu})$ against $|\hat{\mu}|$ together with fits of linear segments obtained for system sizes $L = 13.5, 15.8, 18.0, 20.3, 22.5$ for spherical liquid droplets and bubbles, respectively.

Summarizing, our results clearly demonstrate that within the considered range of radii, $\delta_L(R_s)$ appears to depend markedly on R_s, such that Tolman's hypothesis $\delta_L(R_s) \approx$ const. is ruled out. In particular, this implies that not only the capillarity approximation but even the classical Tolman formula (27) is unmasked as a mere mirage which may only hold in the limit of very large droplet and bubble radii with little physical interest. Still, we cannot resist the temptation to attempt an extrapolation of our findings to $R_s \to \infty$, although—based the accuracy and range of our presently available data—this is obviously a bit presumptuous. Below, we summarize our present attempts in Fig. 16. Of course, we would like to extrapolate the values $\pm\delta^{(L)}(R_s = \infty)$ obtained from the fits of the linear sections of the branches $\delta^{(L)}(R_s)$ for droplets and bubbles, respectively. Even though the two smallest systems were excluded, the data shown in Fig. 8 fail to have a common intersection point at $R_s^{-1} \to 0$. Nevertheless, the crossing points are slightly biased towards negative values, such that one may speculate about a small negative limiting Tolman length. We can do a similar thing for the quotients of the values $\Gamma_s^{(L)}(R_s = \infty)$ obtained as fit parameters from the fits of the linear sections of the adsorption Γ_s (cf. Fig. 12) and the approximate limiting density difference $\pm\Delta\rho(R_s = \infty) \approx \pm 0.682$ (cf. Fig. 13) to $L \to \infty$. As an additional route for a possible extrapolation of $\delta(R_s)$ to $R_s \to \infty$, we have investigated $R_e - R_s$ parametrized by the excess chemical potential $\hat{\mu}$ instead of R_s. As Fig. 14 shows, upon this reparametrization we also find a linear relation between $\delta(\hat{\mu})$ and $\hat{\mu}$ similar to what is observed by Julin *et al.* in Ref. 34. In fact, from comparing our data with those of Fig. 3 in Ref. 34, we are tempted to interpret the slight increase of slope in their data as an onset of the transition from configurations with a single spherical cluster to the homogeneous oversaturated gas. However, with a cutoff of 5σ used in Ref. 34, we are unable to directly verify this suspicion in a quantitative way. Again fitting these linear sections with straight lines and recording the intersections of these lines with the ($\hat{\mu} = 0$)-axis produces another set of finite size estimators for δ, whose behavior turns out to be similar to the one obtained for the quantity $\Gamma_s/\Delta\rho$ in a numerical analysis (see below). From the physical point of view, however, reparametrization of the droplet/bubble formation barrier $\delta\Omega$ by $\widehat{\mu}$ has its merits, since R_s is after all a purely theoretical quantity, whereas the excess chemical potential $\widehat{\mu}$ is more directly related to experiment. From Fig. 3, we see that near its equilibrium coexistence value $\widehat{\mu} = 0$, the excess chemical potential $\widehat{\mu}$ is not plagued by noticeable finite size effects, and Taylor-expanding the *supersaturation*

$$S^{(p)}(\widehat{\mu}) := \frac{p(\widehat{\mu})}{p(\widehat{\mu} = 0)} \approx 1 + \frac{\rho(\widehat{\mu} = 0)}{p(\widehat{\mu} = 0)}\widehat{\mu}, \tag{54}$$

where $\widehat{\mu} = 0$ gives a straight line through 1 with experimentally accessible slope ρ_0/p_0, where ρ_0 and p_0 denote the corresponding coexistence density and pressure, respectively. On the other hand, the equation of state for many supersaturated gases may be approximated by that of an ideal gas, and thus $S^{(p)}(\widehat{\mu}) \approx S^{(\rho)}(\widehat{\mu})$, where

$$S^{(\rho)}(\widehat{\mu}) := \rho(\widehat{\mu})/\rho(\widehat{\mu} = 0). \tag{55}$$

Of course, for our data the relation $\widehat{\mu} \to S^{(\rho)}(\widehat{\mu})$ turns out to be slightly nonlinear. Nevertheless, since Eq. (55) is a convenient parametrization from the experimental point of view, we chose to indicate some of these values in Fig. 15, which shows the free energy barriers $\Delta\Omega^{(L)}(\widehat{\mu})$ as functions of $\widehat{\mu}$. The plot also reminds us once more of the vast overestimation of a naive capillarity approximation.

In summary, the results of the various routes to access the Tolman length for large droplet radii are shown in Fig. 16, in which, however, we have excluded the data for $L = 13.5$ and $L = 15.8$, since these two smallest system sizes did not allow to determine the various extrapolations with sufficient precision. This plot may again hint at a small negative Tolman length for droplets, which we would estimate as $\delta \approx -0.13$. Although with the chosen conditions our present system is far from criticality, it is worth mentioning that this result agrees both in sign and order of magnitude with the mean field prediction for δ at the critical point.[32,38] Furthermore, our result is in nice agreement with other recent estimates[19,34,35] and in particular quite compatible with results from density functional theory as will be shown below, but to be honest, the quality and range of our present data may not be sufficient for any conclusive answer.

In closing this section, we report that for cylindrical phase separation geometry, a similar analysis was also attempted. However, compared to the generic situation encountered in the numerical evaluation of the spherical case, the slopes of $\widehat{\mu}(T, \rho)$ at the corresponding density regions are much gentler (cf. Fig. 5). One may anticipate that this considerably amplifies numerical errors in the evaluation. Furthermore, in addition to finite size effects similar to those discussed above for spherical droplets (or bubbles, respectively),

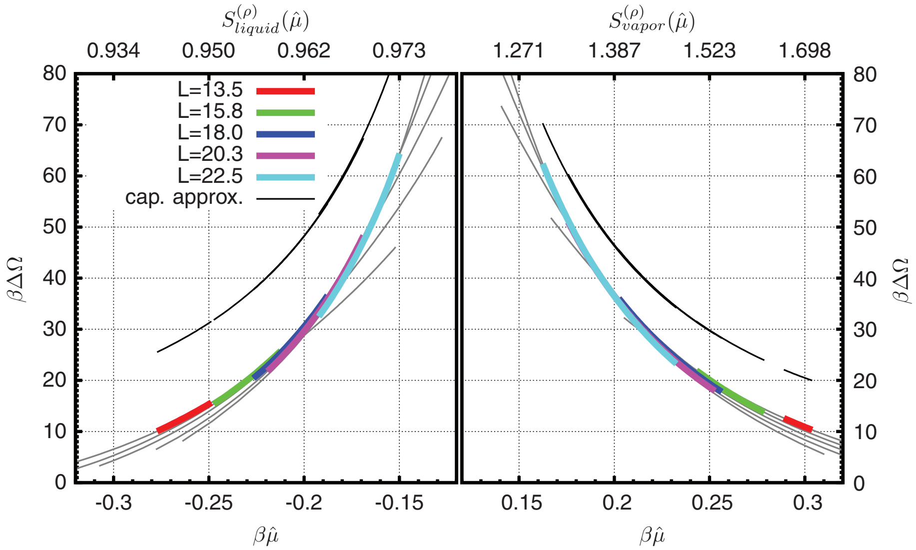

FIG. 15. Dimensionless formation free energy barriers $\beta\Delta\Omega^{(L)}$ as functions of $\widehat{\mu}$ for system sizes $L = 13.5, 15.8, 18.0, 20.3, 22.5$ for spherical vapor bubbles (left) and liquid droplets (right), respectively. On the upper axes, $S^{(\rho)}(\widehat{\mu})$-values of the surrounding liquid and vapor corresponding to the bottom $\hat{\mu}$-labels are indicated for the convenience of the reader. The gross overestimations of the simple capillarity approximation are also shown.

additional finite size effects are to be expected due to the finite length of the cylinders, which constrains capillary wave type fluctuations in the direction parallel to the cylinder axis. As cylindrical phase separation is only invoked by the use of periodic boundary conditions, there is little interest in computing further observables like $\Delta p^{(L)}$ or $\Delta\Omega^{(L)}$ for this case, and the corresponding results are not shown here. Similarly, we have computed $\delta^{(L)}(R_s)$ also for the cylindrical case by applying a 2d version of the above theory. Unfortunately, due to their already mentioned modest accuracy, we can only report that it is difficult to draw any reliable conclusions based on the set of cylindrical data which is currently available to us.

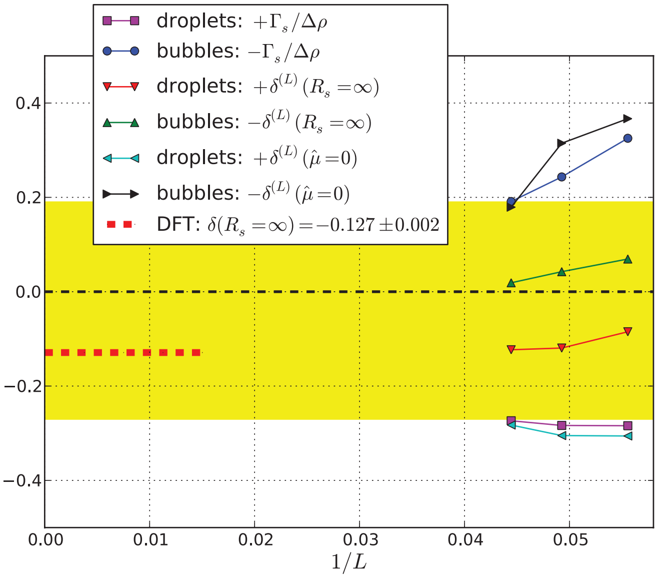

FIG. 16. Attempted finite size extrapolation of the various estimators for the Tolman length. The yellow area serves as a guide to the eye for visualizing a reasonable bound for the asymptotic behavior of the data.

V. RESULTS FROM DENSITY FUNCTIONAL THEORY

In this section, we examine the bubble and droplet formation using density functional theory (DFT) within a mean field approximation for the attractive part of the interaction potential. For simplicity, we will enforce radially symmetric density profiles in a finite box of radius L_{sph}. Therefore, we expect to see a sharp transition from an overcompressed vapor to a spherical liquid bubble (or from a metastable liquid to a spherical vapor bubble) but we will miss the transitions from spherical to cylindrical and cylindrical to slab phases as seen in Figs. 2 and 3. We are not specifically interested in these but rather in a direct comparison with simulations of the density-dependent chemical potential $\mu(\rho)$ in the appropriate domain as well as in the question whether the functions $\delta(R_s; L_{\mathrm{sph}}) = R_e - R_s$ (evaluated for the stable droplets in a finite box and formally dependent on the box size L_{sph}) reduce to a single function, corresponding to the case of the truly metastable droplets in an infinite box.

For a finite box, we take as a constraint that the average density $\bar{\rho}$ in the box is fixed to a certain value ρ_{av}. One can implement this constraint into the minimization of the free energy $\mathcal{F}$ through the definition of a grand potential-like functional

$$\Omega'[\rho] = \mathcal{F}[\rho] - \mu(\rho_{\mathrm{av}}) \int_{L_{\mathrm{sph}}} d\mathbf{r}\rho(r) \tag{56}$$

where the chemical potential $\mu = \mu(\rho_{\mathrm{av}})$ serves as the Lagrange multiplier needed to enforce the constraint. Here, $\int_{L_{\mathrm{sph}}} d\mathbf{r} \ldots = 4\pi \int_0^{L_{\mathrm{sph}}} r^2 dr \ldots$. Thus for the equilibrium profile $\rho_{\mathrm{eq}}(r)$ the following holds:

$$\left.\frac{\delta\Omega'}{\delta\rho(r)}\right|_{\rho(r)=\rho_{\mathrm{av}}(r)} = \left.\frac{\delta\mathcal{F}}{\delta\rho(r)}\right|_{\rho(r)=\rho_{\mathrm{av}}(r)} - \mu(\rho_{\mathrm{av}})\,, \tag{57}$$

$$\int_{L_{\mathrm{sph}}} d\mathbf{r}\rho(r) = \frac{4}{3}\pi L_{\mathrm{sph}}^3\, \rho_{\mathrm{av}}\,. \tag{58}$$

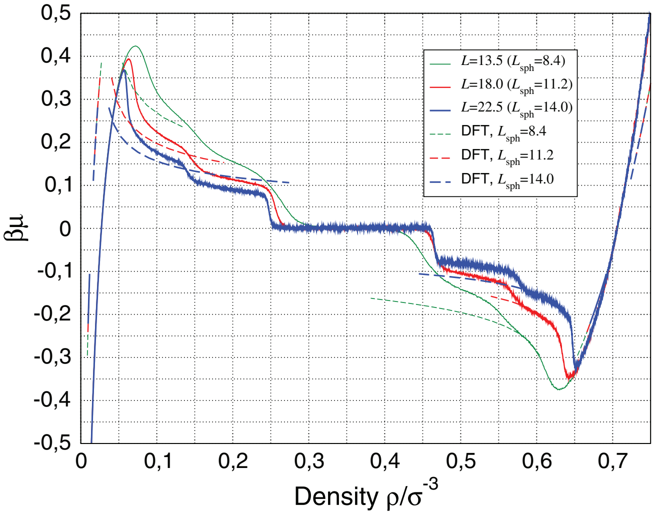

FIG. 17. Comparison between the canonical chemical excess potentials from simulations and DFT. The DFT results have been multiplied with a factor which is the ratio of the planar surface tensions values obtained by simulation and DFT (see text). The radius L_{sph} of the spherical DFT box has been chosen such that the total volume matches the volume L^3 of a cubic simulation box.

The free energy functional used in our computations is spelled out explicitly in our previous paper (see Ref. 35). Basically, we have split $\mathcal{F}[\rho]$ into the sum of the exactly known ideal gas part, a reference hard-sphere part and a mean field part for the attractive part of the intermolecular potential based on a Weeks–Chandler–Andersen (WCA) separation of the cut and shifted Lennard–Jones potential used in our work. The reference hard-sphere functional was treated using fundamental measure theory, see Ref. 35 for all necessary definitions. This functional gives reasonable agreement for the coexistence densities well below the critical point and planar liquid–vapor surface tensions which are about 25% too large (see Tab. I in Ref. 35).

Since $\mathcal{F}[\rho]$ is nonlocal in the density, we need to specify a condition for the density outside the finite, spherical box. We choose the natural bulk condition $\rho(r > L_{\mathrm{sph}}) = \rho(L_{\mathrm{sph}})$.

In Fig. 17, the DFT results for the chemical excess potential $\mu(\rho_{\mathrm{av}}) - \mu_{\mathrm{coex}}$ are compared to the corresponding simulation values for three radii of the spherical box. The radius L_{sph} has been chosen such that $4\pi/3\, L_{\mathrm{sph}}^3 = L^3$, i.e., the system volumes in DFT and simulations are equal. We note that the DFT results have been rescaled with the ratio of the planar surface tensions $\sigma_{\infty,\,\mathrm{sim}}/\sigma_{\infty,\,\mathrm{DFT}} = 0.74$. The reason behind this bases on the observation that the excess free energy in the phase-separated system is essentially proportional to the surface free energy of the droplet/bubble, and the main difference between simulation and DFT for this excess free energy stems from the difference in the planar surface tension values. Since the chemical excess potential is the density derivative of the excess free energy density, the same argument applies to it as well. We see that upon that rescaling the "bubble" part of the chemical excess potential agrees rather well with the simulations, whereas for the "droplet" part the agreement is only qualitative, presumably owing to the rather deficient description of the metastable vapor region.

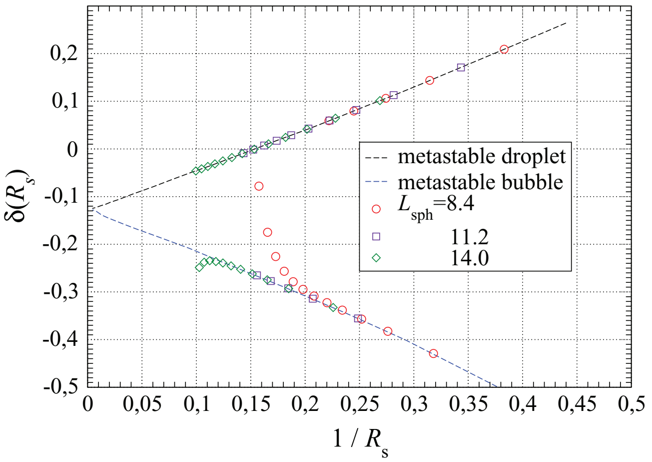

FIG. 18. DFT results for the radius-dependent Tolman length function $\delta(R_s;\, L_{\mathrm{sph}}) = R_e - R_s$ for three box radii L_{sph}. Dashed lines show the corresponding results for the metastable droplets and bubbles, obtained in Ref. 35 using a much larger spherical box.

In Fig. 18, we observe that for droplets, $\delta(R_s;\, L_{\mathrm{sph}})$ evaluated for three different radii L_{sph} all lie on a master curve which is given by the corresponding results for the *meta*stable droplets obtained in Ref. 35. For bubbles, deviations from the master curve are visible for bubble radii $\gtrsim L_{\mathrm{sph}} - 3$. These deviations are due to the stronger correlations in the liquid. Nevertheless, it seems that DFT results are rather robust against variation of the system size, in contrast to the simulation results. At present, it is however not clear inasmuch this behavior would change by using also a cubic box for DFT (or a spherical box in the simulations). Therefore, attributing the differences between simulation and DFT to the fluctuations certainly missed by DFT is questionable.

In Fig. 19, we present a direct comparison of our estimates for the radius-dependent Tolman length $\delta(R_s;\, L_{\mathrm{sph}}) = R_e - R_s$ as obtained from simulations and DFT calculations. It is remarkable that even though the DFT result obviously displays a markedly different slope as a function of $1/R_s$

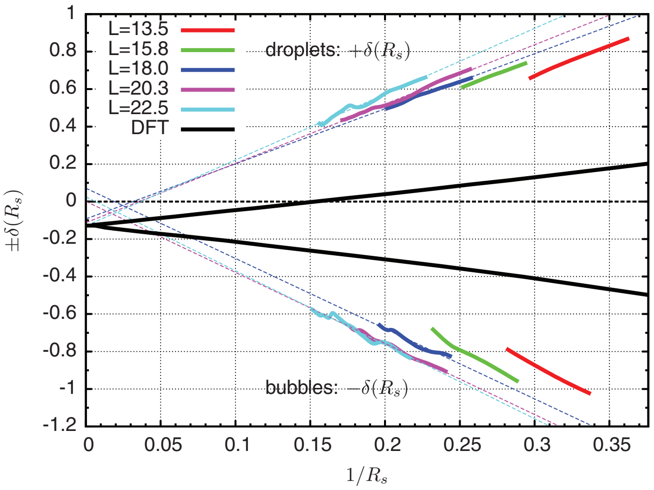

FIG. 19. Comparison of results for the radius-dependent Tolman length $\delta(R_s;\, L_{\mathrm{sph}}) = R_e - R_s$ as obtained from simulations and DFT calculations.

as compared to the simulation data, the limiting behavior of the two sets of data seems to be compatible, as was already observed in our previous work.[35]

We have also compared the DFT results for the adsorption Γ_s at the surface of tension to those of the simulation. The qualitative findings are similar to the case of $\delta(R_s)$, namely that overall the DFT values for Γ_s are smaller than those observed in simulation, and that the DFT droplet results for Γ_s all collapse on a single master curve. However, the bubble results show a strong spread due to finite size effects. Thus, here the extrapolation of the DFT results to $R_s \to \infty$ would also be difficult, similar as in the simulation case.

VI. DISCUSSION

In the present work, for the vapor–liquid transition of fluids we have presented a method to study the free energy of droplets and bubbles as a function of their radius for the physically relevant range of nucleation barriers ($10 \leq \beta\Delta\Omega^* \leq 65$, cf. Fig. 11). Our method does not need any atomic geometric criterion to distinguish atoms (or molecules) that are inside or outside the droplet (or bubble, respectively), but relies exclusively on a phenomenological analysis of two-phase equilibria inside finite volumes. The thermodynamic functions of such fluids (in practice, we study here only the Lennard–Jones model with truncated and shifted interactions at a single temperature of about 78% of the critical temperature) are obtained very precisely with umbrella sampling methods for a broad range of system volumes (cf. Figs. 2 and 3).

In our approach, we determine both the equimolar radius R_e as well as the radius R_s of the surface of tension (see Fig. 6). We are then able to obtain the radius-dependent interface tension $\sigma_s(R_s)$ at the surface of tension (Fig. 9), the Laplace pressure difference (Fig. 10), and the difference $\Delta\rho$ of the bulk densities of both phases (Fig. 13). These data clearly show that in the range of interest significant deviations from the capillarity approximation $\sigma(R_s) \approx \sigma_\infty$ occur; the capillarity approximation always yields an overestimate in the range of interest. For droplets, the deviations are in the range from 5% to 20%; for bubbles, in the range from 10% to 30%. At the same value of R_s, the deviation for bubbles is always significantly larger than for droplets. If these trends would persist up to $R_s \to \infty$, the Tolman length clearly would have to assume a nonzero limiting value. For the R_s-dependent "effective" Tolman length $\delta(R_s) = R_e - R_s$ for droplets, one finds a positive but strongly R_s dependent result of the order of 0.5σ in the accessible range (Fig. 8), but taken together with the information from the bubbles it is likely that for $R_s \to \infty$ a slightly negative Tolman length (of the order of 0.1σ) will result. These numbers may nevertheless deviate from those of other works, since, e.g., the values obtained for the surface tension are known to strongly depend on the chosen Lennard–Jones cutoff.[39,40]

It is interesting to note that density functional theory, employing a standard mean field treatment of the interparticle attractions, yields a much weaker dependence of $\sigma_s(R_s)$ and $\delta(R_s)$ on R_s although the limiting behavior for $R_s \to \infty$ agrees with the simulation results.

The uncertainty in determining the limit δ_∞ from our data is in part due to the limiting system sizes that are available for the Lennard–Jones system in combination with a reasonable computational effort. On the other hand, as the free energy data show, the asymmetry in the free energy, which, as we have mentioned above, is a necessary ingredient for a nonzero limiting value δ_∞ is not very pronounced for the present model. A tailor-made system to observe a nonzero limit of the Tolman length should thus be computationally as cheap as possible, and should involve a pronounced asymmetry between condensed and vapor phase, and indeed the corresponding results on an Ising model with three-spin interaction are much more conclusive.[41]

Unfortunately, we also observed considerable finite-size effects in the analysis, which add to the difficulties of making any conclusive statement about the limiting value of the Tolman length. We must stress that the origin of these finite size deviations, which were not anticipated in the context of first order transitions, are currently not well understood. For instance, as one can recognize from Fig. 9, the branches $\sigma_s^{(L)}$ derived from the indicated different choices of L do not perfectly collapse onto an L-independent "master curve." Instead, there occurs a slight but systematic mismatch. These finite-size effects can have several reasons: On the one hand, due to the finite linear dimension L of the box, a droplet (or bubble, respectively) interacts with its "images" created by the periodic boundary conditions via long range density fluctuations. On the other hand, other observables, e.g., the densities of the pure phases at the chosen chemical potential are found to be only slightly L-dependent. In fact, when one analyzes the states where a droplet (or bubble, respectively) coexists with the corresponding surrounding bulk phase, one has strong fluctuations of the observables of interest ($\hat{f}_L, \hat{\mu}_L, R_s, R_e, \ldots$). Some of these observables presumably exhibit distributions that are not symmetric with respect to their mean, and such an asymmetry is expected to lead to systematic errors in the data such as shown in Figs. 9 and 12. New simulation results for two-dimensional systems suggest that these finite size effects are even more pronounced in two than in three dimensions.[42] More work to clarify these effects is desirable.

We have investigated also the appearance of finite size effects in our density functional calculations by using a spherical box having a radius with size comparable to the linear dimensions used in the simulations. Interestingly, for droplets a perfect data collapse independent of the box size is found; for bubbles, some systematic deviations occur, but only when the bubble radius comes close to the box radius. Thus it would be desirable to use such a spherical geometry also for the simulations (with the obvious advantage that in such a setting systematic effects due to transitions to cylindrical droplets are not expected). Conversely, a DFT study reconsidering the problem in a cubic instead of a spherical box would be equally useful. These approaches must be left for future work, however. Finally, we stress that the problems to carry out a reliable extrapolation to accurately estimate the Tolman length do not at all prevent us from making reasonably accurate predictions for nucleation barriers as function either of the droplet (or bubble) radius (Fig. 11) or of the chemical potential difference (or supersaturation, respectively), see Fig. 15. We have shown that the classical capillarity approximation overestimates these barriers strongly.

ACKNOWLEDGMENTS

We are grateful to B. Evans, A. Shchekin, and in particular to J. Henderson and D. Kashchiev for helpful correspondence, and acknowledge support by the Austrian Science Fund (FWF) Project P22087-N16 and by the Deutsche Forschungsgemeinschaft (DFG) through the Priority Program SPP 1296 (Heterogeneous Nucleation). A.T. would like to thank D. Reith for valuable computer support.

[1] D. W. Oxtoby, J. Phys.: Condens. Matter **4**, 7627 (1992).
[2] J. L. Katz, Pure Appl. Chem. **64**, 1661 (1992).
[3] P. G. Debenedetti, *Metastable Liquids* (Princeton University, Princeton, NJ, 1996).
[4] D. Kashchiev, *Nucleation: Basic Theory with Applications* (Butterworth Heinemann, Oxford, UK, 2000).
[5] M. P. Anisimov, Russ. Chem. Rev. **72**, 591 (2003).
[6] O. Penrose and J. Lebowitz, J. Stat. Phys. **3**, 211 (1971).
[7] O. Penrose and J. Lebowitz, *Towards a Rigorous Molecular Theory of Metastability* (North Holland, Amsterdam, 1987), Chap. 5.
[8] K. Binder and M. H. Kalos, J. Stat. Phys. **22**, 363 (1980).
[9] M. Schrader, P. Virnau, and K. Binder, Phys. Rev. E **79**, 061104 (2009).
[10] K. Binder, Physica A **319**, 99 (2003).
[11] A. Tröster, C. Dellago, and W. Schranz, Phys. Rev. B **72**, 094103 (2005).
[12] A. Tröster, Phys. Rev. B **76**, 012402 (2007).
[13] K. Binder and D. Stauffer, Adv. Phys. **25**, 343 (1976).
[14] K. Binder, Rep. Prog. Phys. **50**, 783 (1987).
[15] R. C. Tolman, J. Chem. Phys. **16**, 758 (1948).
[16] R. C. Tolman, J. Chem. Phys. **17**, 118 (1949).
[17] R. C. Tolman, J. Chem. Phys. **17**, 333 (1949).
[18] E. M. Blokhuis and J. Kuipers, J. Chem. Phys. **124**, 074701 (2006).
[19] A. E. van Giessen and E. M. Blokhuis, J. Chem. Phys. **131**, 164705 (2009).
[20] S. Ono and S. Kondo, *Molecular Theory of Surface Tension in Liquids*, Handbuch der Physik Vol. 10 (Springer, Berlin, 1960), pp. 134–280.
[21] J. Rowlinson and B. Widom, *Molecular Theory of Capillarity* (Dover, New York, 1982).
[22] V. I. Kalikmanov, *Statistical Physics of Fluids* (Springer, Berlin, 2001).
[23] H. Vehkamaki, *Classical Nucleation Theory in Multicomponent Systems* (Springer, Berlin/Heidelberg/New York, 2006).
[24] T. L. Hill, J. Chem. Phys. **56**, 526 (1952).
[25] T. F. Nonnenmacher, Chem. Phys. Lett. **47**, 507 (1977).
[26] S. Rekhviashvili and E. Kishtikova, Tech. Phys. Lett. **32**, 439 (2006).
[27] S. Rekhviashvili, E. Kishtikova, R. Karmokova, and A. Karmokov, Tech. Phys. Lett. **33**, 48 (2007).
[28] S. Rekhviashvili and E. Kishtikova, Tech. Phys. **56**, 143 (2011).
[29] C. Borgs and R. Kotecky, J. Stat. Phys. **61**, 79 (1990).
[30] A. M. Ferrenberg and R. H. Swendsen, Phys. Rev. Lett. **61**, 2635 (1988).
[31] P. Virnau and M. Müller, J. Chem. Phys. **120**, 10925 (2004).
[32] M. P. A. Fisher and M. Wortis, Phys. Rev. B **29**, 6252 (1984).
[33] K. Koga, X. C. Zeng, and A. K. Shchekin, J. Chem. Phys. **109**, 4063 (1998).
[34] J. Julin, I. Napari, J. Merikanto, and H. Vehkamaki, J. Chem. Phys. **133**, 044704 (2010).
[35] B. J. Block, S. K. Das, M. Oettel, P. Virnau, and K. Binder, J. Chem. Phys. **133**, 154702 (2010).
[36] E. M. Blokhuis and D. Bedeaux, Physica A **184**, 42 (1992).
[37] T. V. Bykov and A. K. Shchekin, Inorg. Mater. **35**, 641 (1999).
[38] M. P. Anisimov, Phys. Rev. Lett. **98**, 035702 (2007).
[39] M. J. P. Nijmeijer, A. F. Bakker, C. Bruin, and J. H. Sikkenk, J. Chem. Phys. **89**, 3789 (1988).
[40] Y. A. Lei, T. Bykov, S. Yoo, and X. C. Zeng, J. Am. Chem. Soc. **127**, 15346 (2005), see http://pubs.acs.org/doi/pdf/10.1021/ja054297i.
[41] A. Tröster and K. Binder, Phys. Rev. Lett. **107**, 265701 (2011).
[42] A. Tröster and K. Binder, “Microcanonical determination of the interface tension of flat and curved interfaces from Monte Carlo simulations,” J. Phys.: Condens. Matter (to be published).